Characterization of an InAs/GaSb type-II superlattice barrier photodetector operating in the LWIR domain

Rodolphe Alchaar, Jean-Baptiste Rodriguez, L. Höglund, S. Naureen, Philippe Christol

Characterization of an InAs/GaSb type-II superlattice barrier photodetector operating in the LWIR domain

Cite as: AIP Advances **9**, 055012 (2019); https://doi.org/10.1063/1.5094703
Submitted: 05 March 2019 . Accepted: 30 April 2019 . Published Online: 15 May 2019

R. Alchaar, J. B. Rodriguez, L. Höglund, S. Naureen, and P. Christol

Characterization of an InAs/GaSb type-II superlattice barrier photodetector operating in the LWIR domain

Cite as: AIP Advances 9, 055012 (2019); doi: 10.1063/1.5094703
Submitted: 5 March 2019 • Accepted: 30 April 2019 •
Published Online: 15 May 2019

R. Alchaar,[1] J. B. Rodriguez,[1] L. Höglund,[2] S. Naureen,[2] and P. Christol[1,a)]

AFFILIATIONS

[1]IES, Univ. Montpellier, CNRS, F-34000 Montpellier, France
[2]IRnova AB, Electrum 236 - C5, SE-164 40 Kista, Sweden

[a)]**Corresponding author: Tel.:** (+33) 467 143 822; **e-mail address:** christol@ies.univ-montp2.fr

ABSTRACT

In this paper, structural, optical and electrical characterizations of longwave infrared barrier detectors based on the InAs/GaSb superlattice are reported and analyzed. The fabricated detectors exhibited a 50% cut-off wavelength around 10.5 µm at 80K measured by photoluminescence and spectral response. The dark current density was 8.4×10^{-4} A/cm^2 at 80K and a performance analysis combining spectral response, dark current-voltage characteristic and capacitance-voltage measurement curves was performed to determine the operating bias and the dark current regimes at different biases. Dark current simulations were also performed to better understand limiting dark current mechanisms of the device performance.

I. INTRODUCTION

There has been growing interest in the InAs/GaSb type-II superlattice (T2SL) for infrared detection, especially for long-wave infrared (LWIR) detection suitable for space applications.[1,2] Its high uniformity, bandgap adjustability, low Auger recombination rate and high carrier effective mass make this material a potential alternative to well-established materials for high performance cooled IR detector such as mercury cadmium telluride (MCT).

Another important feature of the T2SL material is the possibility of implementing it in a barrier structure, where a unipolar barrier blocks one carrier type and allows the flow of the other. This barrier allows suppressing the electric field-related Shockley-Read-Hall (SRH) recombination, leading to a reduced dark current compared to a simple PIN junction.[3] The structure reported in this work is based on a double heterostructure barrier design with a contact layer made of a n-type InAs/GaSb SL, a barrier made of an InAs/AlSb SL and a p-type doped InAs/GaSb SL absorber. Due to the p-type doping in the absorber, the electrons are the minority carriers which have higher diffusion length than holes, yielding a higher quantum efficiency.[4,5] The barrier, made of InAs/AlSb, is tailored to have a large offset in the valence band and minimal offset in the conduction band, therefore blocking majority holes and collecting photo-generated electrons. Similar Ga-containing InAs/GaSb LWIR barrier photodetectors have already been studies in several research groups.[6–9]

In this paper, we report the characterization an InAs/GaSb T2SL barrier photodetectors operating in the LWIR spectral range. The measurements include dark current density-voltage characteristics (J-V), capacitance-voltage (C-V) and spectral response. Combining analysis of experimental curves, one can extract the operating bias and the dark current regimes at different biases of the devices. In addition to the electrical measurements and to better understand the device performance, dark current simulations were performed using the software SILVACO ATLAS which has already been used for midwave infrared photodetectors.[10,11] ATLAS is a commercially available software used to simulate device performances by solving differential equations derived from Maxwell's equations, such as continuity and transport equations. By fitting the simulated dark current to the experimental data, we can estimate previously

unknown material parameters such as the minority carrier lifetime, their effective mass and trap energy level within the bandgap. This fitting provides a complementary tool to identifying limiting factors of the device performance.

II. SIMULATION MODEL

ATLAS uses derivations based on the Boltzmann transport theory to approximate the current densities by a drift-diffusion model:[12]

$$J_{n,p} = q(n,p)\mu_{n,p}E \pm qD_{n,p}\nabla_{n,p} \quad (1)$$

where J represents the current density, q the electronic charge, μ the mobility, E the electric field, D the diffusion constant, ∇ is the gradient and n, p are the electron and hole concentrations, respectively.

The dark current in a barrier structure is mainly limited by the diffusion current at low reverse bias whatever the temperature, but as the reverse bias increases, the depletion region widens and depletes the barrier. When the bias is large enough, the depletion region reaches the absorber, and the junction-related electric field activates mid-gap traps causing the appearance of generation-recombination (GR) and trap-assisted tunneling (TAT) currents. The Hurkx model allows us to combine the GR and TAT current contributions into one expression:[13–17]

$$R_{SRH} = \frac{pn - n_i^2}{\frac{\tau_p}{1+\Gamma_p}\left[n + n_i \exp\left(\frac{E_{trap}}{kT_L}\right)\right] + \frac{\tau_n}{1+\Gamma_n}\left[p + n_i \exp\left(\frac{-E_{trap}}{kT_L}\right)\right]} \quad (2)$$

where R_{SRH} is the SRH recombination rate, n_i is the intrinsic carrier concentration, E_{trap} is the energy difference between the trap energy level inside the bandgap and the intrinsic Fermi level, k is Boltzmann's constant, T is the lattice temperature, τ_n and τ_p are the electron and hole carrier lifetimes, respectively, and they are set as equal in the model. The intrinsic carrier concentration is given by:

$$n_i = \sqrt{N_c N_v}\exp\left(\frac{-E_g}{2kT_L}\right) \quad (3)$$

E_g is the bandgap energy, $N_{c,v}$ is the electrons or holes density of states, in the bulk approximation:

$$N_{c,v} = 2\left(\frac{2.\pi.m^*_{e,h}.k.T_L}{h^2}\right)^{\frac{3}{2}} \quad (4)$$

$m^*_{e,h}$ is the electron or hole effective mass and h is Planck's constant.

The field enhancement factor $\Gamma_{n,p}$ is given by:

$$\Gamma_{n,p} = \frac{\Delta E_{n,p}}{kT_L}\int_0^1 \exp\left(\frac{\Delta E_{n,p}}{kT_L}u - K_{n,p}u^{\frac{3}{2}}\right)du \quad (5)$$

where u is the integration variable, $\Delta E_{n,p}$ is the energy range where tunneling can occur for electrons or holes, and $K_{n,p}$ is defined as:

$$K_{n,p} = \frac{4}{3}\frac{\sqrt{2.m_t.\Delta E_{n,p}^3}}{q\hbar|E|} \quad (6)$$

with m_t being the tunneling effective mass, E the electric field and ħ the reduced Planck's constant.

The combined GR and TAT current density therefore becomes:

$$J_{GR+TAT} = q\int_W R_{SRH}dy \quad (7)$$

W being the depletion region width.

By implementing the drift-diffusion and Hurkx models in ATLAS, we can have an accurate description of the main components of the dark current for LWIR barrier detectors. Moreover, the main goal of the simulation is to extract material parameters that cannot be directly measured with our setup. These parameters are present in the above equations and can be input in ATLAS, such as the n-type and p-type carrier lifetimes τ_n and τ_p, respectively, the trap energy level E_{trap} and the tunneling mass m_t. These parameters are initially estimated based on the literature or taken as weighted averages of binary material parameters proposed by the ATLAS manual,[18] and then fine-tuned until we reach an agreement between the simulation and the experimental data. The parameters chosen for our simulation are summarized in Table I with their respective references.

TABLE I. Material parameters used for the simulation.

Electron effective mass (x m_0)[24,25]	0.04
Hole effective mass (x m_0)[24]	0.75
Permittivity	15.3
Electron affinity (eV)[7]	4.73
Electron mobility (cm^2/V s)[14]	1000
Hole mobility (cm^2/V s)[14]	500
Nominal bandgap at 80K (eV)	0.1181

III. BARRIER STRUCTURE DESIGN

The LWIR barrier structure shown in this study consists of lightly p-type doped 3.2 μm-thick InAs/GaSb SL, with a composition of 15 monolayers (MLs) of InAs and 7 MLs of GaSb, which should exhibit a cut-off wavelength around 11 μm at 80K. The top contact is a heavily n-type doped wide bandgap InAs/GaSb SL, and the barrier is a lightly n-type doped SL. The role of the barrier is to block majority holes from reaching the contact layer, so it must be thick enough to prevent the holes from tunneling back and forth to the absorber layer. In addition, it must be high enough to block the thermionic emission coming from the contact layer, while allowing the minority electrons to flow unhindered. In order to have a barrier in the valence band, we have chosen the InAs/AlSb SL as a material for the barrier layer with a composition of 16.5 MLs of InAs and 4 MLs of AlSb. Finally, the bottom contact layer consists of a wide bandgap heavily p-type doped InAs/GaSb SL.

Figure 1 shows a band diagram corresponding to the previously described barrier structure, simulated with ATLAS at 80K, using material parameters of Table I and under no bias. The structure is designed so that the electric field will be confined inside the barrier meaning that the absorber will not be depleted under low reverse bias. As a consequence, the GR current is greatly suppressed leading to a diffusion-limited current performance whatever the temperature.

The diffusion dark current in the absorbing layer depends on the majority doping concentration, which in our case is p-type, so the doping level N_{dop} has to be chosen to optimize the diffusion

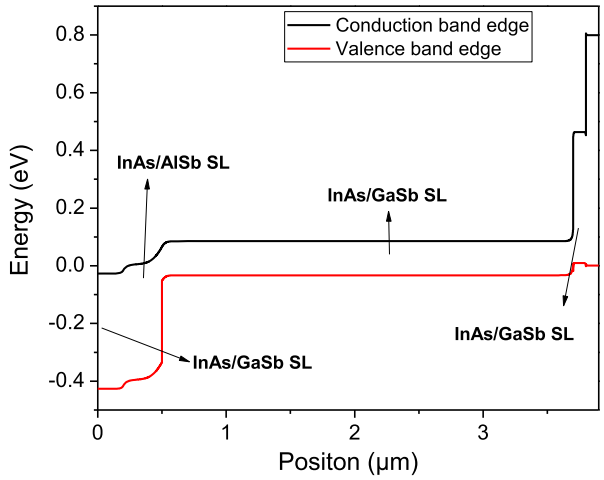

FIG. 1. Simulated band diagram of the barrier structure at 80K and 0V.

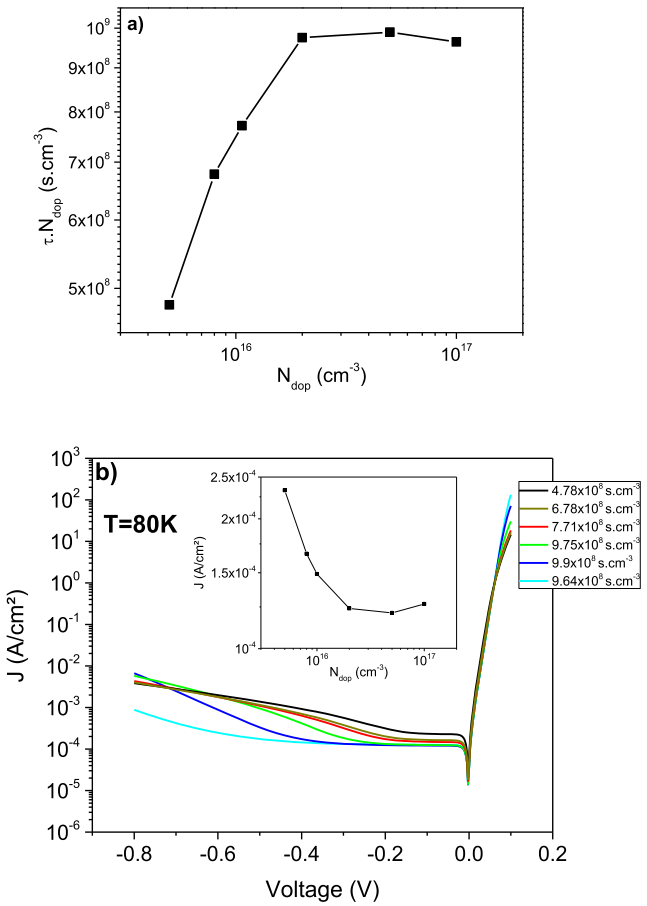

FIG. 2. (a) $\tau.Nd_{op}$ product as a function of N_{dop}; (b) Dark current simulations with different absorber $\tau.Nd_{op}$ product values; the inset shows dark current density extracted at -100 mV as a function of N_{dop}.

current equation in the following approximation:

$$J_{diff} = q\frac{n_i^2.L}{\tau.N_{dop}} \tag{8}$$

where L is the absorber's thickness or the minority carrier diffusion length, whichever is shorter.

According to eq. 8, the $\tau.N_{dop}$ product has to be maximized in order to have the lowest diffusion current. Previous experimental and theoretical studies were carried out to understand the influence of intentional doping on the carrier lifetimes in InAs/GaSb SLs.[19,20] A set of dark current simulations were performed using ATLAS, with $\tau.N_{dop}$ product values extracted from Reference 20 and shown in figure 2a. The doping was varied from 5×10^{15} to 1×10^{17} cm^{-3} and the corresponding carrier lifetimes were calculated from Reference 20. The resulting current density-voltage curves are shown in figure 2b, and the current density was extracted from each curve at -100 mV and plotted against the doping concentration in the inset of figure 2b. The current density decreases between 5×10^{15} and 5×10^{16} cm^{-3} and then increases after that. From these simulations, a doping concentration of about $4\text{-}5\times10^{16}$ cm^{-3} showed the optimal performance, and was therefore chosen for the absorbing layer.

IV. FABRICATION AND CHARACTERIZATION

The LWIR T2SL barrier structure was grown by solid source molecular beam epitaxy (MBE) on n-type GaSb substrates. Figure 3a displays the high-resolution x-ray diffraction (HRXRD) spectrum, showing a structure lattice matched to the GaSb substrate. Moreover, the presence of numerous and intense satellite peaks is a signature of high quality structure. Measured period thickness is equal to 6.7 nm, in agreement with the nominal thickness for the absorbing layer. Atomic force microscopy was used to investigate the surface morphology, and we found a root mean square roughness of 0.13 nm for a surface of 2×2 μm^2 as shown in figure 3b.

For the photoluminescence (PL) measurements, a piece of sample was etched down to the absorber. The measurement is therefore performed directly on the absorbing layer. Figure 4 shows a PL measurement at 80K with a peak position at 10.5 μm, and the inset shows the variation of the PL peak energy as a function of temperature. From these curves, we can extract the bandgap energy as well as its temperature dependence using the Varshni relation:[21,22]

$$E_g(T) = E_g(0) - \frac{\alpha.T^2}{\beta + T} \tag{9}$$

where $E_g(T)$ is the bandgap energy at temperature T, α is a fitting parameter and β is a constant. The value of β was set at 270K,[23] and the Varshni fitting allowed us to extract the values of α and $E_g(0)$ which were 1.678×10^{-4} eV/K and 0.12195 eV, respectively.

LWIR T2SL devices were then fabricated following a 5 steps optical photolithography procedure. Prior to the fabrication, the samples are sequentially cleaned by acetone, ethanol and isopropyl alcohol and dried with N_2. The first step is the Ti/Au deposition by electron beam evaporation for the top contacts, followed by an acetone lift-off. The second step is the shallow chemical etching of circular mesas with a usual acid-based solution.[24] The etching depth is subsequently determined using a profilometer. Since the device is shallow-etched, surface leakage current on the

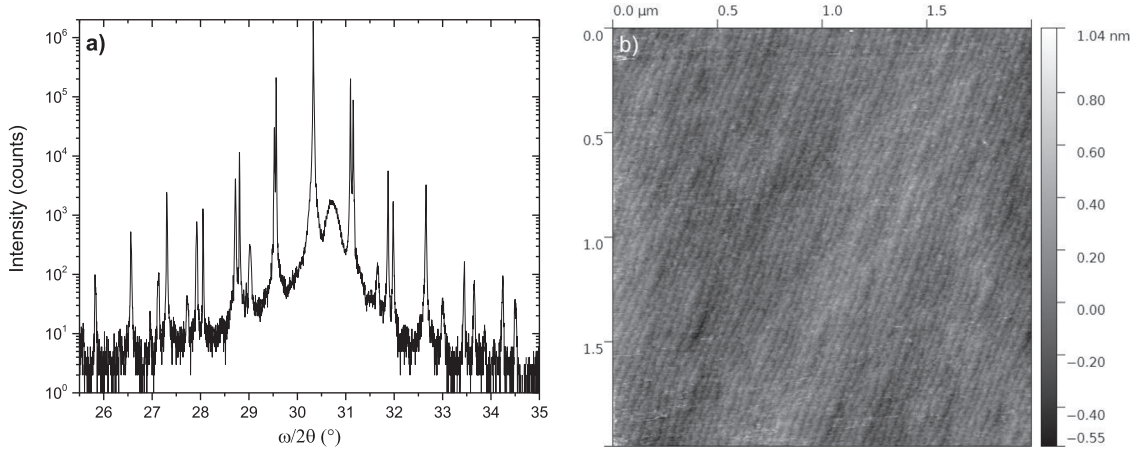

FIG. 3. (a) High resolution XRD spectrum of the grown T2SL barrier structure; (b) 10×10 µm^2 AFM image of the surface morphology.

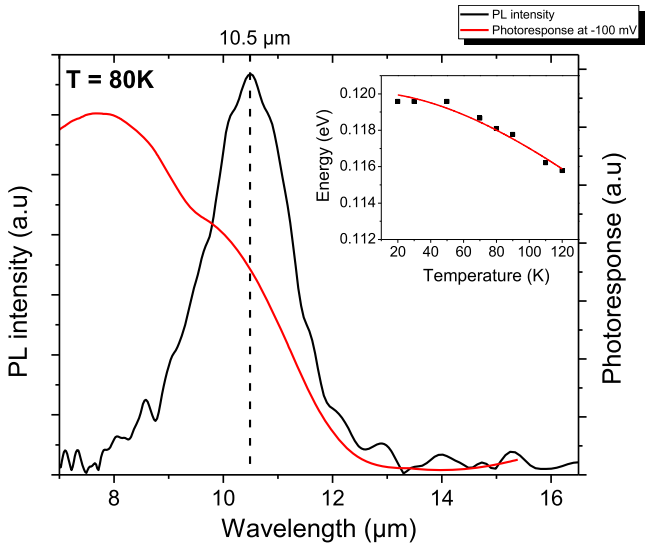

FIG. 4. Photoresponse and photoluminescence measurements at 80K. The inset shows the variation of the PL peak in function of the temperature and the red line represents the Varshni fitting.

etched sidewalls is suppressed. A polymerized photoresist layer was used for protection and electrical insulation of the mesa. The step that follows is another etching, with the same chemical solution as the second step, to reach the bottom contact layer. Finally, a Ti/Au layer was deposited for the contact pads and the bottom contacts.

V. ELECTRICAL CHARACTERIZATION AND DARK CURRENT REGIMES IDENTIFICATION

The sample was then bonded onto a 68-pin leadless chip carrier and mounted into a Janis cryostat to perform non-calibrated spectral photoresponse (PR) measurements. Figure 4 shows the front side illuminated spectral PR spectrum at -100 mV in addition of the PL measurement spectrum. One can see that the PL peak at 10.5 µm is close to the 50% cut-off wavelength for the spectral PR, slightly lower than the expected theoretical value. The spectral PR spectra obtained at different biases and at 80K are shown in Figure 5a. Next, the samples are mounted in a cryogenic probe station to perform the current density-voltage (J-V) and capacitance-voltage measurements (C-V). Figure 5b shows the J-V curves at temperatures ranging from 20 to 160K, performed on a detector with a 210 µm-diameter. At low temperature, until 70K, the dark current is limited by the photonic current due to the experimental set-up. The Arrhenius plot in figure 5c shows the dark current density at -100 mV versus 1/T. A fitting was done over the range 80-160K using the expression $CT^3\exp(-E_a/kT)$,[25] which resulted in an activation energy of E_a=117.85 meV (C is a fitting constant), close to the measured bandgap energy at 80K (118.1 meV), indicating a diffusion-limited behavior down to 80K. The dark current starts to deviate from the linear trend below 80K, which could be attributed to the photonic current caused by the residual photonic emission coming from the measurement setup. R_dA product values were extracted from dark current measurements at 80K and -100 mV and plotted against the perimeter to area ratio in figure 5d. R_d represents the differential resistance, calculated from the derivative of the voltage over the current and A is the device area. A linear fit was performed and the R_dA product shows almost no size dependence, indicating the absence of leakage current.

Figures 6a, 6b, 6c and 6d show the normalized PR, dark current density, R_dA product and $(C_{surf})^{-2}$ measurements as a function of the voltage, respectively, and obtained from the same device at 80K. The PR values were extracted from the spectral photoresponse measurements at different biases and at 10.5 µm. $(C_{surf})^{-2}$ represents the inverse square surface capacity $(A/C)^2$ extracted from the C-V measurement. From $(C_{surf})^{-2}$=f(V) we can extract the doping by fitting equation 9 to the linear part of the curve:

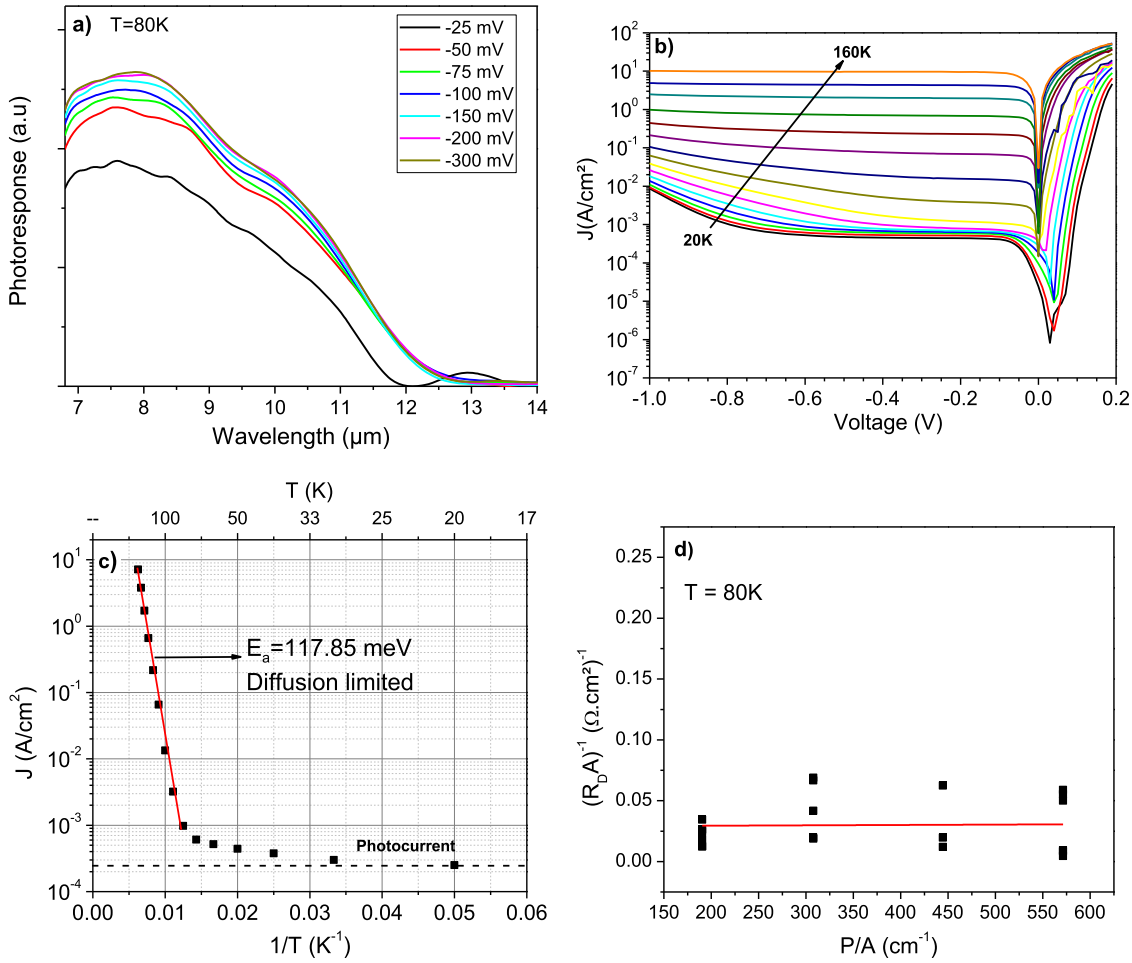

FIG. 5. (a) Photoresponse measurements at different biases; (b) current density-voltage measurements at different temperatures; (c) Arrhenius plot at -100 mV; (d) R_DA as a function of P/A and the linear fitting.

$$\left(\frac{A}{C}\right)^2 = \frac{2}{q\epsilon_0\epsilon_{SL}}\left(\frac{V_d - V}{N_{dop}}\right) \tag{10}$$

where ε_0 is the vacuum permittivity, ε_{SL} is the permittivity of the superlattice, considered to be 15.3 for the InAs/GaSb SL and 14.84 for the InAs/AlSb SL, V_d is the diffusion potential in the junction and N_{dop} is the intentional doping concentration.

If we closely examine the shape of the displayed curves, we can identify three main dark current regimes:

i) The device becomes fully turned on at -100 mV (where R_dA is at maximum value), the diffusion plateau is reached and the PR value saturates. The depletion region is still confined within the barrier. We will define -100 mV as the operating bias V_{OP}.

ii) At -300 mV, GR current starts to appear. At this point, the barrier is fully depleted and the depletion region reaches the absorber, which explains the appearance of the electric field-related GR current. We will define V_{GR}=-300 mV.

iii) At stronger reverse bias, the depletion region widens inside the absorber, and at around -530 mV the trap-assisted tunneling current appears. The -530 mV bias will be designated as V_{TAT}.

This analysis will be useful for the doping extraction from the $(C_{surf})^{-2}$ curve, because it allows us to pinpoint the position of the depletion region at different biases. Therefore, we can safely assume that between 0 and -300 mV the depletion region is confined inside the barrier and the doping extracted in this range will be that of the barrier, and from -300 mV onwards, the extracted doping corresponds to the absorber. The values we found were around 1.2×10^{16} cm^{-3} for the absorber, lower than the targeted optimized value, and 1.3×10^{16} cm^{-3} for the barrier, close to the chosen value.

From this analysis we were able to evaluate the operating bias of the device, which was -100 mV, slightly higher than expected. At this operating bias, dark current density value as low as 8×10^{-4} A/cm^2 and R_dA product as high as 1160 Ω.cm^2 were extracted at 80K.

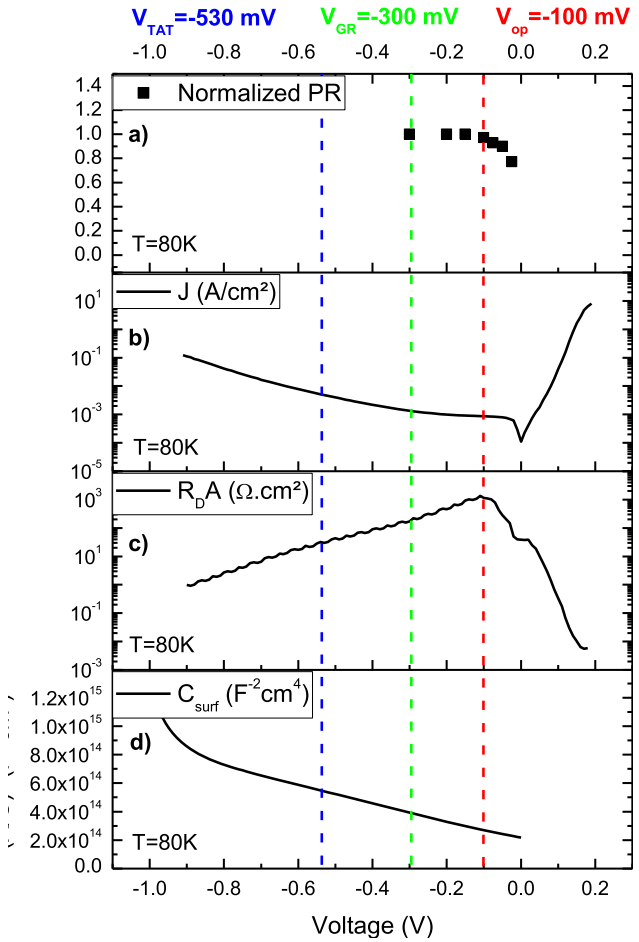

FIG. 6. Stacking of the experimental (a) normalized photoresponse, (b) current density, (c) R_DA and (d) surface capacity as a function of the voltage at 80K.

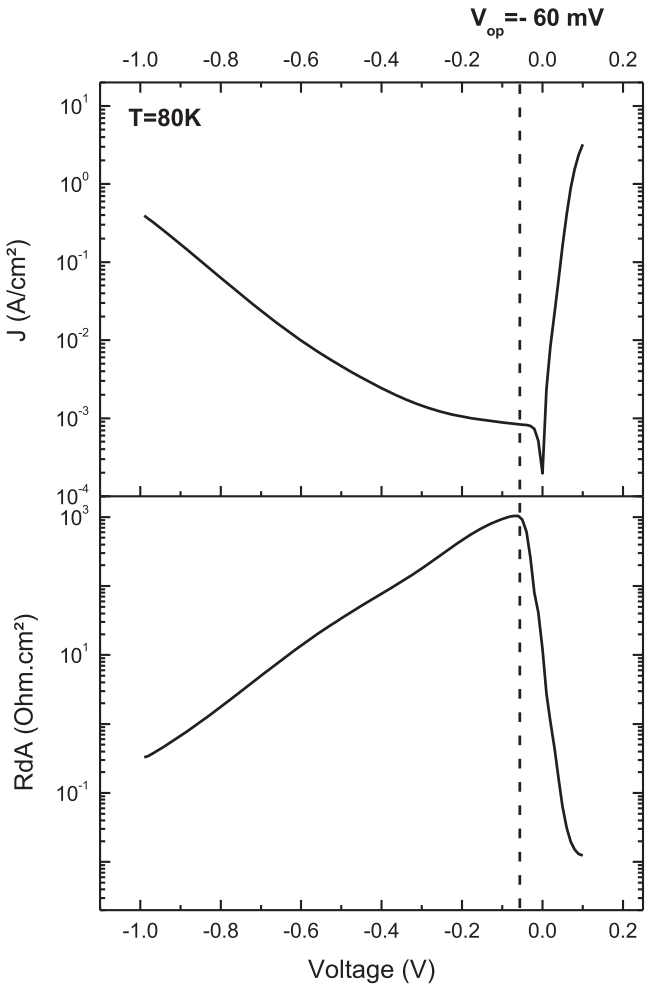

FIG. 7. Stacking of the experimental current density and R_DA curves as a function of the voltage, measured on the optimized device at 80K.

These results at 100mV in reverse bias at 80K, for a detector device having cut-off wavelength of 10.5µm, are analogous to the ones reported by Manurkar *et al.* for a device showing a 50% cutoff wavelength of 11µm at 81K.[7] A similar analysis was performed on the simulated dark current in figure 2b, and an operating bias of -55 mV was found with an absorber doping of 5×10^{16} cm^{-3}. A reasonable explanation to this difference in operating biases between simulation and experiment would be that minority electrons are being blocked by a small barrier in the conduction band, resulting from a band bending at the barrier/absorber interface. Therefore, electrons need higher reverse bias to overcome this barrier, leading to a higher operating bias. In order to mitigate this issue, a second generation structure was grown, having a different barrier design with a barrier doping of 5×10^{15} cm^{-3}, and the same fabrication and characterization steps were performed on the new sample. Figure 7 shows the experimental J-V and R_dA curves for the sample at 80K. The operating bias was estimated using the same method as in figure 6. The new design yielded an operating bias of -60 mV, lower than that of the first generation design and closer to the simulation, with a dark current value equal to 8.4×10^{-4}A/cm^2. For that reason, we have decided to move forward with this design for future devices.

In order to correlate the dark current regimes observed in figure 6 with the model described in the second section, we performed a set of dark current simulations at different temperatures and compared them to experimental results. The doping data obtained from C-V measurements were inserted into the simulation software, as well as bandgap energy values and Varshni parameters obtained from PL for bandgap temperature dependence modeling (inset of Fig. 4). The remaining experimentally unknown, user-defined parameters required for the simulation were the carrier lifetime $\tau_{n,p}$, electron and hole effective masses $m^*_{e,h}$, tunneling effective mass m_t and the trap energy level inside the bandgap E_t. We started by setting the carrier lifetime to 30 ns at 80K, as reported in the literature for LWIR InAs/GaSb SL from time resolved photoluminescence measurements.[26,27] Then, the electron and hole effective masses were also taken from the literature to be equal to $0.04m_0$

and $0.75m_0$, respectively, for similar materials.[28,29] Equation 4 was used to calculate the valence and conduction band density of states with these effective masses. The other unknown parameters were adjusted until we had a good fit between experimental and simulated curves. The tunneling mass was $0.023m_0$ and the trap energy level was found to be located 12 meV above the intrinsic Fermi level, near 2/3 of the bandgap energy. Simulation results are shown in figure 8a, and were compared to experimental measurements from figure 6b in the temperature range 80-140K, where the dark current is undisturbed by the photonic current. A good agreement between simulation and experiment can be seen, which proves the accuracy of the chosen model and material parameters. The carrier lifetime was adjusted to fit the measurements at each temperature

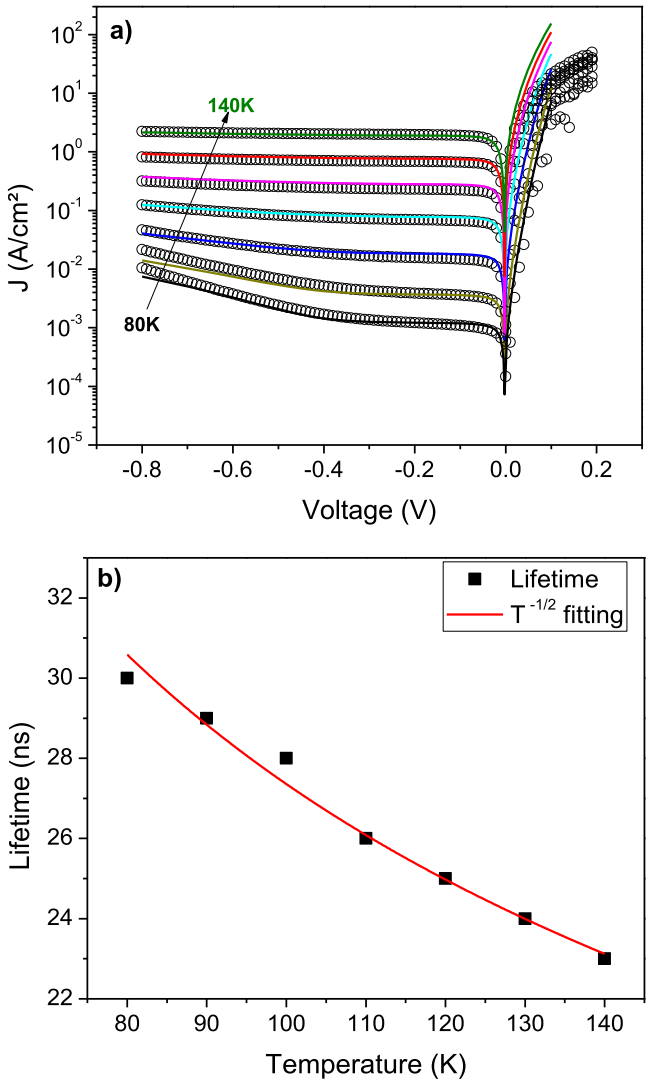

FIG. 8. (a) measured and simulated current density curves at different temperatures; (b) minority carrier lifetimes extracted from the simulations at different temperatures with the $T^{-1/2}$ fitting.

TABLE II. Material parameters extracted from the experimental measurements and the simulations.

Electron and hole lifetimes @80K (ns)	30
Tunneling effective mass (x m_0)	0.023
E_{trap} (eV)	0.012
E_g (eV) at 80K	0.1181
α (eV/K)	1.678×10^{-4}
β (K)	270

while m_t and E_t were kept constant. Figure 8b shows the variation of the carrier lifetime in function of the temperature. A fitting was added to the curve showing that the lifetime follows a $T^{-1/2}$ trend, characteristic of a SRH-limited lifetime in this temperature range.[11,26] When the minority carrier lifetime is assumed to be SRH dominated with a value of about 30 ns at 80K, the dark current is almost 1.5 orders of magnitude above the MCT benchmark "Rule 07".[30] The material parameters extracted from the experimental measurements and the simulations for the LWIR InAs/GaSb T2SL barrier photodetector are summarized in Table II.

VI. CONCLUSION

In conclusion, we have reported the characterization of LWIR infrared barrier detector based on the InAs/GaSb T2SL. The detector showed a cut-off wavelength around 10.5 µm at 80K, confirmed by photoluminescence and spectral photoresponse measurements, with low dark current and diffusion-limited behavior down to 80K. Capacitance-voltage measurements allowed us to confirm the doping in the structure. The dark current measurements were then analyzed to identify different current mechanisms in the structure and to estimate the operating bias. The operating bias (-100mV) was slightly higher than expected, and this issue was reduced to -60 mV by adjusting the band alignment between the absorber and barrier layers. At this operating bias, dark current density equal to 8.4×10^{-4}A/cm^2 was extracted at 80K. By identifying and modeling the different dark current contributions using the software SILVACO, carrier lifetime value of about 30 ns was extracted from experimental curves at 80K, explaining in part that dark current density value is as high as 1×10^{-3} A/cm^2 at this temperature.

ACKNOWLEDGMENTS

This work was partially funded by the French "Investment for the Future" program (EquipEx EXTRA, ANR 11-EQPX-0016) and ESA contract n°4000116260/16/NL/BJ.

REFERENCES

[1]K. Minoglou, N. Nelms, A. Ciapponi, H. Weber, S. Wittig, B. Leone, and P. E. Crouzet, "Infrared image sensor developments supported by the European Space Agency," Infrared Physics & Technology **96**, 351–360 (2019).
[2]M. Sakai, J. Murooka, A. Kumeta, T. Kimura, H. Inada, Y. Iguchi, Y. Hiroe, and M. Kimata, "Development of Type-II superlattice VLWIR detectors in JAXA," Proc. SPIE Infrared Technology and Applications XLIII **10177**, 1017714 (2017).
[3]S. Maimon and G. Wicks, "nBn detector, an infrared detector with reduced dark current and higher operating temperature," Appl. Phys. Lett. **89**(15), 151109 (2006).

[4]D. Hoffman, B.-M. Nguyen, P.-Y. Delaunay, A. Hood, M. Razeghi, and J. Pellegrino, "Beryllium compensation doping of InAs/GaSb infrared superlattice photodiodes," Appl. Phys. Lett. **91**(14), 143507 (2007).
[5]E. Giard, I. Ribet-Mohamed, M. Delmas, J. B. Rodriguez, and P. Christol, "Influence of the p-type doping on the radiometric performances of MWIR InAs/GaSb superlattice photodiodes," Infrared Physics & Technology, **70**, 103–106 (2015).
[6]B.-M. Nguyen, D. Hoffman, E. K.-W. Huang, P.-Y. Delaunay, M. Razeghi, and J. Hubbs, "Background limited long wavelength infrared type-II InAs/GaSb superlattice photodiodes operating at 110 K," Appl. Phys. Lett. **93**, 123502 (2008).
[7]P. Manurkar, S. Ramezani-Darvish, B.-M. Nguyen, M. Razeghi, and J. Hubbs, "High performance long wavelength infrared mega-pixel focal plane array based on type-II superlattices," Appl. Phys. Lett. **97**, 193505 (2010).
[8]B. Rafol, A. Soibel, A. Khoshakhlagh, J. Nguyen, J. K. Liu, J. M. Mumolo, S. A. Keo, L. Hoglund, D. Z. Ting, and S. D. Gunapala, "Performance of a 1/4 VGA format long-wavelength infrared antimonides-based superlattice focal plane array," IEEE J. Quantum Electronics **48**, 878 (2012).
[9]Z. Xu, J. Chen, F. Wang, Y. Zhou, Z. Bai, J. Xu, Q. Xu, C. Jin, and L. He, "MBE growth and characterization of type-II InAs/GaSb superlattices LWIR materials and photodetectors with barrier structures," J. Crystal Growth **477**, 277 (2017).
[10]J. Abautret, J. P. Perez, A. Evirgen, F. Martinez, P. Christol, J. Fleury, H. Sik, R. Cluzel, A. Ferron, and J. Rothman, "Electrical modeling of InSb PIN photodiode for avalanche operation," J. Appl. Phys. **113**(18), 183716 (2013).
[11]M. Delmas, J.-B. Rodriguez, and P. Christol, "Electrical modeling of InAs/GaSb superlattice mid-wavelength infrared pin photodiode to analyze experimental dark current characteristics," J. Appl. Phys. **116**(11), 113101 (2014).
[12]S. Selberherr, *Analysis and simulation of semiconductor devices*, Springer Science & Business Media (2012).
[13]W. Shockley and W. T. Read, "Statistics of the recombinations of holes and electrons," Physical Review **87**(5), 835–842 (1952).
[14]R. N. Hall, "Electron-hole recombination in germanium," Physical Review **87**(2), 387 (1952).
[15]G. A. M. Hurkx, H. C. de Graaf, W. J. Kloosterman, and M. P. G. Knuvers, "A new analytical diode model including tunneling and avalanche breakdown," IEEE Trans. Electron Devices **39**(9), 2090–2098 (1992).
[16]F. Callewaert, A. M. Hoang, and M. Razeghi, "Generation-recombination and trap-assisted tunneling in long wavelength infrared minority electron unipolar photodetectors based on InAs/GaSb superlattice," **104**(5), 053508 (2014).
[17]G. A. M. Hurkx, D. B. M. Klaassen, and M. P. G. Knuvers, "A new recombination model for device simulation including tunneling," IEEE Trans. Electron Devices **39**(2), 331–338 (1992).
[18]Silvaco. Users manual. 2016; Available from: https://dynamic.silvaco.com/dynamicweb/jsp/downloads/DownloadManualsAction.do?req=silentmanuals&nm=atlas.
[19]S. Bandara, P. G. Maloney, N. Baril, J. G. Pellegrino, and M. Z. Tidrow, "Doping dependence of minority carrier lifetime in long-wave Sb-based type II superlattice infrared detector materials," Optical Engineering **50**(6), 061015 (2011).
[20]M. Kopytko and A. Rogalski, "HgCdTe barrier infrared detectors," Progress in Quantum Electronics **47**, 1–18 (2016).
[21]Y. P. Varshni, "Temperature dependence of the energy gap in semiconductors," Physica **34**(1), 149–154 (1967).
[22]C. Cervera, I. Ribet-Mohamed, R. Taalat, J. P. Perez, P. Christol, and J. B. rodriguez, "Dark current and noise measurements of an InAs/GaSb superlattice photodiode operating in the midwave infrared domain," Journal of Electronic Materials **41**(10), 2714–2718 (2012).
[23]B. Klein, E. Plis, M. N. Kutty, N. Gautam, A. Albrecht, S. Myers, and S. Krishna, "Varshni parameters for InAs/GaSb strained layer superlattice infrared photodetectors," J. Phys. D: Appl. Phys. **44**(7), 075102 (2011).
[24]R. Chaghi, C. Cervera, H. Aït-Kaci, P. Grech, J. B. Rodriguez, and P. Christol, "Wet etching and chemical polishing of InAs/GaSb superlattice photodiodes," Semicond. Sci. Technol. **24**(6), 065010 (2009).
[25]D. R. Rhiger, E. P. Smith, B. P. Kolasa, J. K. Kim, J. F. Klem, and S. D. Hawkins, "Analysis of III–V superlattice nBn device characteristics," Journal of Electronic Materials **45**(9), 4646–4653 (2016).
[26]B. C. Connelly, G. D. Metcalfe, H. Shen, and M. Wraback, "Direct minority carrier lifetime measurements and recombination mechanisms in long-wave infrared type II superlattices using time-resolved photoluminescence," Appl. Phys. Lett. **97**(25), 251117 (2010).
[27]D. Donetsky, G. Belenky, S. Svensson, and S. Suchalkin, "Minority carrier lifetime in type-2 InAs–GaSb strained-layer superlattices and bulk HgCdTe materials," Appl. Phys. Lett. **97**(5), 052108 (2010).
[28]J. Nguyen, D. Z. Ting, C. J. Hill, A. Soibel, S. A. Keo, and S. D. Gunapala, "Dark current analysis of InAs/GaSb superlattices at low temperatures," Infrared Physics & Technology, **52**(6), 317-321 (2009).
[29]J. Pellegrino and R. DeWames, "Minority carrier lifetime characteristics in type II InAs/GaSb LWIR superlattice $n^+\pi p^+$ photodiodes," Proc. SPIE **7298**, 72981U (2009).
[30]D. Rhiger, "Performance comparison of long-wavelength infrared type II superlattice devices with HgCdTe," Journal of electronic materials **40**(8), 1815–1822 (2011).